


## Article

# Axial Compression Behavior of Steel Angle-Corrugated Steel Plate-Confined Concrete Columns

Zexuan Sun<sup>1</sup>, Yun Zou<sup>1,\*</sup>, Chengquan Wang<sup>2</sup> , Jie Pan<sup>1</sup> and Li Wang<sup>1</sup><sup>1</sup> School of Environmental & Civil Engineering, Jiangnan University, Wuxi 214122, China<sup>2</sup> College of Engineering, Zhejiang University City College, Hangzhou 310015, China

\* Correspondence: zouyun\_22@126.com

**Abstract:** This paper proposes a novel type of steel angle-corrugated steel plate-confined concrete column (SA-CS column). The axial compression behavior of the SA-CS column was investigated by load experiments and finite element (FE) simulation. The study also compared the load–displacement curves, core concrete strength index, and specimens’ ductility indices between the SA-CS columns and concrete-filled steel tube (CFST) columns. The results indicated that the mechanical properties of the SA-CS column were better than those of the CFST column with a similar steel ratio. The rationality and reliability of the finite element model were confirmed by comparing the experimental results’ load–displacement curves and failure modes. Based on the FE model, a supplementary parametric analysis of the effects of the compressive strength of core concrete, thickness, yield strength, and wave height of the corrugated steel plate, thickness, and yield strength of the steel angles was conducted. Moreover, some existing design codes were assessed based on the numerical results available in this study. A new calculating model for the SA-CS column was proposed, which is capable of reasonably predicting the numerical results.

**Keywords:** corrugated steel plate; axial load experiment; finite element simulation; parametric analysis; bearing capacity calculation



**Citation:** Sun, Z.; Zou, Y.; Wang, C.; Pan, J.; Wang, L. Axial Compression Behavior of Steel Angle-Corrugated Steel Plate-Confined Concrete Columns. *Appl. Sci.* **2022**, *12*, 10819. <https://doi.org/10.3390/app122110819>

Academic Editor: Omar AlShawa

Received: 5 October 2022

Accepted: 22 October 2022

Published: 25 October 2022

**Publisher’s Note:** MDPI stays neutral with regard to jurisdictional claims in published maps and institutional affiliations.



**Copyright:** © 2022 by the authors. Licensee MDPI, Basel, Switzerland. This article is an open access article distributed under the terms and conditions of the Creative Commons Attribution (CC BY) license (<https://creativecommons.org/licenses/by/4.0/>).

## 1. Introduction

Concrete-filled steel tube (CFST) members have convenient manufacturing and construction properties, high bearing capacity, good seismic performance and ductility, and economic advantages. Square CFST columns are widely used in long-span and heavily-loaded structures due to the benefits of their flexible joint types, larger moment of inertia, and the ease of satisfying construction requirements [1–3]. Scholars have conducted a great deal of research on the performance of square CFST columns, including with regard to their static behaviors [4,5], seismic behaviors [6], fire-resistant performance [7], and creep performance [8]. Compared with circular CFST columns, the confinement of square CFST columns to core concrete is reduced. The external steel tube of square CFST columns can suffer local buckling because of its low out-of-plane stiffness under axial compression, which reduces its bearing capacity.

To improve the confinement effect of square CFST columns and tube wall-buckling resistance, scholars have proposed various new structures to enhance square CFST columns. Gan et al. [9] presented a new type of stiffened square CFST column with diagonal binding ribs, which can increase the effectively confined regions of core concrete from the strengthened tube. A total of 21 stub columns were tested under axial compression to investigate the effect of the diagonal ribs on the mechanical properties of the new type column. Tao et al. [10,11] conducted a series of investigations of concrete-filled, stiffened thin-walled steel tubular columns under axial and eccentric compression through tests and finite element simulation. The results showed that the stiffened column has higher serviceability benefits than those unstiffened, and the carrying capacity of the stiffened column and

confinement of the core concrete increases with the stiffener number. Yang et al. [12] introduced binding bars into square CFST columns to postpone the local buckling of steel tubes and conducted axial compressive tests. In addition, Wang et al. [13] tested square CFST columns with binding bars under cyclic lateral loads to study their hysteretic behavior. The experimental results demonstrated that binding bars do not improve the bearing capacity of specimens significantly but can greatly improve their ductility and energy-dissipation capacity. In addition to these improvement schemes, some scholars used FRP [14] and steel fiber-reinforced concrete [15] to enhance the mechanical behaviors of square CFST columns.

Currently, corrugated steel plates, a type of cold-formed steel plate, are chiefly used in the shear wall and composite beam for their excellent shear resistance [16,17]. The vertical stiffness of corrugated steel plates is low, and it is difficult for them to bear a vertical load due to their particular corrugated form. However, several investigations have shown that corrugated steel plates are favorable for confining concrete and that composite concrete-filled columns with corrugated steel behave well [18–20]. Wang et al. [19] tested a new kind of spiral concrete-filled corrugated steel tube (CFCST) column under axial compression and compared the mechanical properties of the CFCST and CFST columns. The test results demonstrated that the axial compression behavior of the CFCST column was greater than that of the CFST column under a similar steel ratio. Fang et al. [21] performed experimental studies on concrete-filled double-skin steel tubular (CFDST) columns with galvanized corrugated steel tubes and CFCST columns embedded with structural steel (CFCST-S). The existing studies mainly focus on circular concrete-filled columns with corrugated steel tubes. However, like the circular CFST column, a circular concrete-filled column with a corrugated steel tube also suffers from the same problem of a difficult joint connection. In addition, as the internal concrete and corrugated steel tube cannot bear the tensile stress, it is necessary to embed the structural steel or longitudinal bars inside the column to ensure the structure's bending performance, which undoubtedly increases the difficulty of construction. Thus, the research group designed a new type of S-CSC column consisting of corrugated steel plates, steel tubes, core concrete, and concrete in steel tubes. The S-CSC column has been applied in actual projects because of its advantages with respect to its good bending resistance, easy connection, and lack of embedded longitudinal bars, as shown in Figure 1 [22].

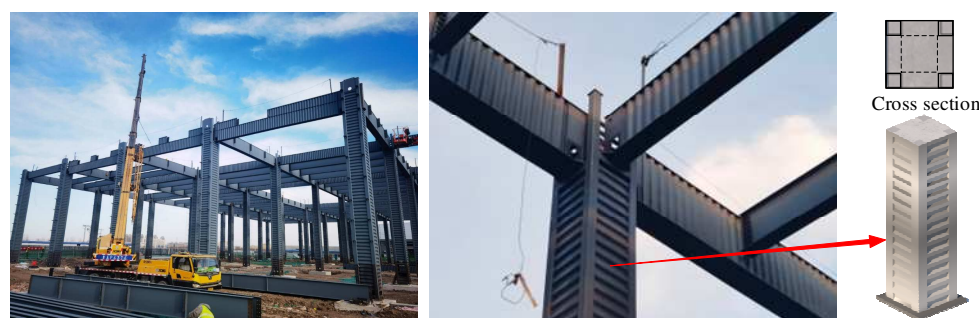


**Figure 1.** Application of S-CSC column [22].

However, to ensure the compactness of concrete in the steel tubular structure, the S-CSC column must maintain a large section size, which makes it unsuitable for civil buildings. In order to solve this problem, the steel tubular design was replaced by steel angles, and a novel type of steel angle-corrugated steel plate-confined concrete column (SA-CS column) was proposed in this paper. The SA-CS column consists of an outer steel skeleton formed by the welding of the steel angle and corrugated steel plate as well as poured core concrete, as shown in Figure 2. The steel angles are placed outward to provide a plane that can be welded with the corrugated steel plates. Whereas the steel angles projecting inwards and corrugated steel plates cannot form a completely closed cavity. Considering the primary function of the steel angle is to connect with the corrugated steel plate, bearing a small part of the bearing capacity, the effect of lateral buckling on the

bearing capacity of the SA-CS column is negligible. Thus, the scheme wherein the steel angles are projecting inward is adopted. The corrugated steel plate is welded horizontally with the steel angle to ensure that the corrugated steel plate's trough and the steel angle's inner edge are in the same plane. Due to the omission of the steel tubular structure, the size limit of the SA-CS column is relaxed, and it is suitable for buildings with small sizes. The purpose of this paper is to propose a new structural form to improve the disadvantages of S-CSC columns that are not suitable for civil buildings. The attempt will provide a new idea for structural design and enable the popularization of structures with corrugated steel plates.

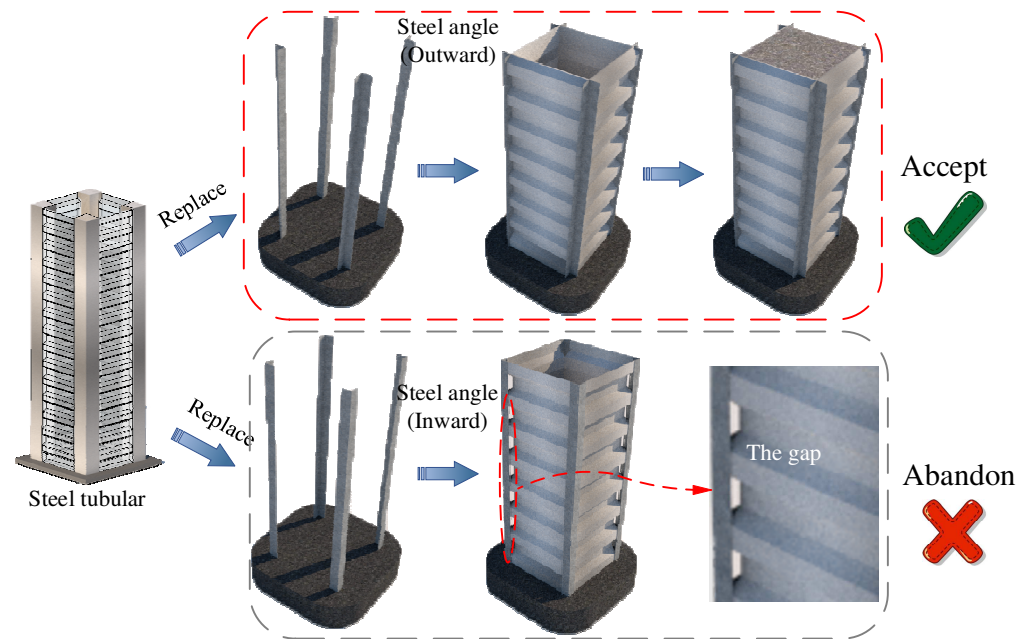


**Figure 2.** Form of SA-CS column.

In this paper, experiments and finite element simulation evaluated the axial compression behavior of the SA-CS column. On this basis, a parameter analysis was supplemented to explore the primary role of each part of the specimen. Finally, we compare the numerical results with the calculated results by some existing codes and propose a newly designed method for predicting the ultimate bearing capacity of the SA-CS column.

## 2. Experimental Programs

### 2.1. Specimen Design and Material Properties

A total of four short columns of 700 mm in length were tested under monotonic axial loads, including three SA-CS columns and one CFST column. The specimens were named SA-CS-230, SA-CS-280, SA-CS-330, and CFST-1. The corrugated steel plates and steel angles of the SA-CS columns had the same wall-thickness ( $t_1$  and  $t_2$ ) of 2 mm, and the wave height ( $h$ ) of the corrugated steel plates for all specimens was 20 mm. The experimental variables of the SA-CS columns were the width of the corrugated steel plate ( $B$ ), whose values were 230 mm, 280 mm, and 330 mm. The dimensions of the steel angle were 30 mm × 30 mm × 2 mm. For CFST-1, the width ( $B_0$ ) and thickness ( $t_0$ ) of the steel tube were 230 mm and 2 mm, respectively. Figure 3 and Table 1 illustrate the detailed parameters of the specimens.

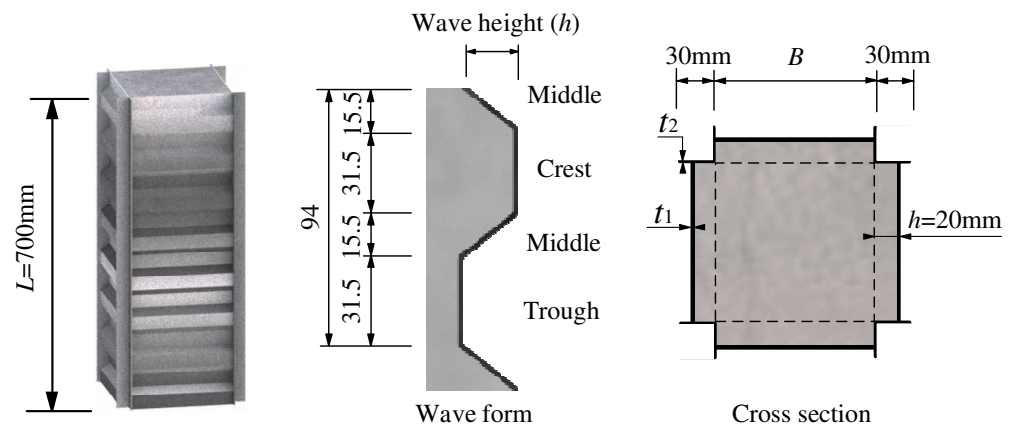


Figure 3. Waveform and cross-section of SA-CS column.

Table 1. Design parameters of specimens.

Specimen Designation	B (mm)	t <sub>1</sub> (mm)	t <sub>2</sub> (mm)	h (mm)	f <sub>cu</sub> (MPa)	f <sub>y</sub> (Mpa)	f <sub>u</sub> (Mpa)	E <sub>s</sub> (Gpa)
SA-CS-230	230	2	2	20				
SA-CS-280	280	2	2	20	35.4	324	363	202
SA-CS-330	330	2	2	20				
	B <sub>0</sub> (mm)		t <sub>0</sub> (mm)					
CFST-1	230		2		35.4	324	363	202
CFST-2	230		2		44.4	347	425	206

Commercial concrete was used for the specimens, and six concrete blocks with dimensions of 150 mm × 150 mm × 150 mm, under the same curing conditions as the specimens, were tested under axial loading to obtain the compressive strength. The measured compressive strength ( $f_{cu}$ ) was 35.4 Mpa [23]. The steel angles, corrugated steel plates, and steel tubes were all made of Q345 steel. Tensile tests of the steel were carried out; the measured yield strength ( $f_y$ ) was 324 Mpa, the measured ultimate strength ( $f_u$ ) was 363 Mpa, and the measured elastic modulus ( $E_s$ ) was 202 Gpa. The corresponding yield strain was 1928  $\mu\epsilon$  [24].

In order to make the test results more reliable, this paper also compared the axial compression test results of the CFST column by Yao et al. [25]. The length and cross-section dimensions of the specimen tested by Yao were the same as those of CFST-1. The specimen was named CFST-2. Table 1 also lists the material properties of CFST-2.

### 2.2. Test Method

The specimens were tested under a 10,000 kN hydraulic testing machine applying the method of displacement loading, whose loading increment was 2 mm/min. The test terminated when the loading capacity of the specimen dropped to 75% of its peak load or the apparent physical failure of the specimen occurred. Two linear variable displacement transducers (LVDTs) were placed at the angles of the loading plates of the columns to monitor the degree of vertical displacement. Meanwhile, vertical and transverse strain gauges were arranged in the middle span of the columns to measure the strains of the steel angle and corrugated steel plate. Figure 4 shows the details of the test and measuring equipment.



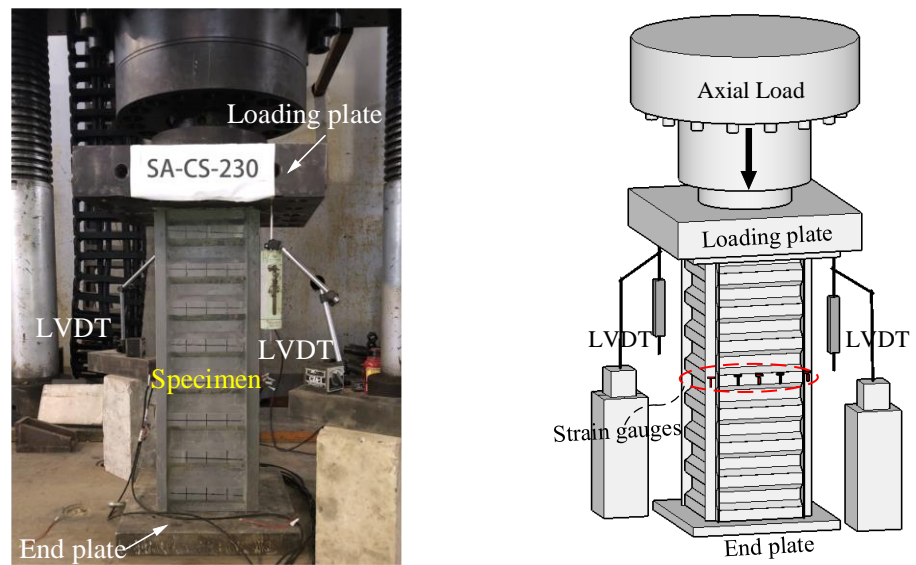


Figure 4. Test and measuring equipment.

### 3. Experimental Results and Discussion

#### 3.1. Failure Modes

Figure 5a plots the failure modes of the SA-CS columns. The specimens were under the elastic phase at the initial loading stage, and no evident phenomena were observed. With the increase in the axial load, the strain of the steel angle developed rapidly, and the local buckling of the steel angle occurred while reaching about 85% of the peak load. After reaching the ultimate bearing capacity, the local buckling of the steel angle developed more severely, and the crest of the corrugated steel plate bulged. At the end of the test, we cut down the corrugated steel plate to observe the failure mode of the core concrete. It was found that the concrete at the trough was crushed while that at the crest had spalled. The specimens did not appear to undergo shear failure due to the excellent confinement effect of the outer steel skeleton.

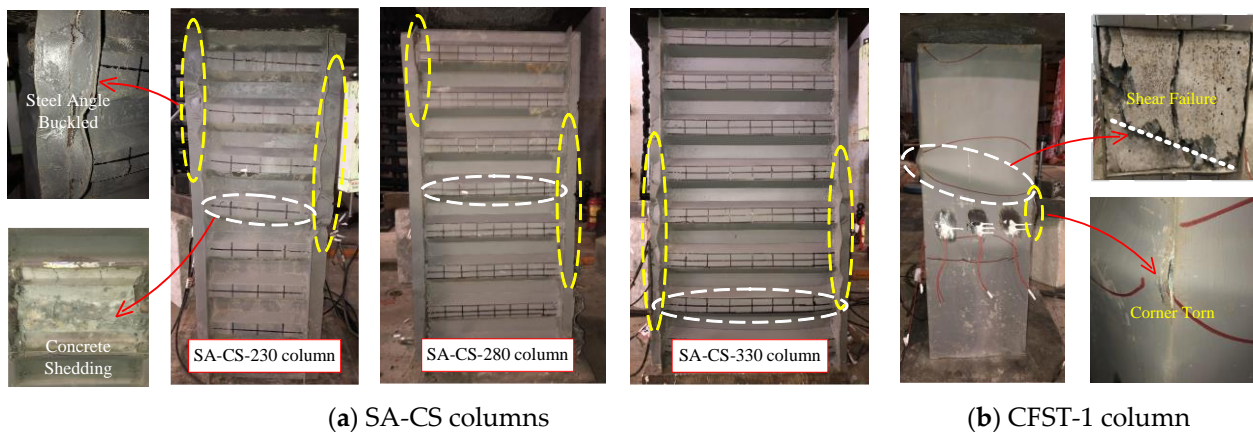


Figure 5. Failure modes of specimens.

For the CFST-1 column, the steel tube buckling occurred at the specimen’s middle height when the load reached 70% of the peak load. The steel tube buckled more severely due to the load increases, and it yielded while reaching the peak load. Finally, the corner of the steel tube was torn, and the test terminated. After cutting the steel tube, the internal concrete was found to occur in diagonal cracks, a typical shear failure. The failure modes of the CFST-1 column are shown in Figure 5b.

### 3.2. Load–Axial Displacement Curves

Figure 6 shows the forms of the load–axial displacement curves of the SA-CS columns and the CFST-1 column, which were similar. The value of the ultimate bearing capacity ( $N_u$ ) and corresponding displacement ( $\Delta_u$ ) of the specimens are also illustrated in Figure 6. The  $N_u$  and  $\Delta_u$  of the two types of columns were not compared in this section due to the different section sizes, and only the load–axial displacement curves of the SA-CS columns with varying section widths were compared. According to the information in the figure, it can be seen that both the bearing capacity and deformation capacity of the specimens improved with the increase in the section width. Compared with the SA-CS-230 column, the  $N_u$  and  $\Delta_u$  of the SA-CS-280 column improved by 38.24% and 5.96%, and those of the SA-CS-330 column enhanced by 85.32% and 14.51%, respectively.

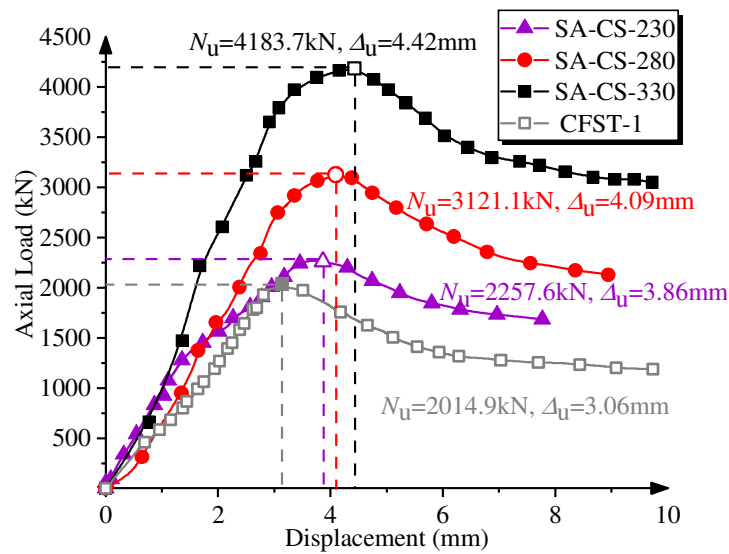


Figure 6. Load-axial displacement curves.

Regarding the CFST-2 column, this section does not compare its load–displacement curves due to the different material properties. The  $N_u$  and  $\Delta_u$  of the CFST-2 column were 1813.5 kN and 1.18 mm, respectively.

### 3.3. Load–Strain Curves of Steel Angle and Steel Tube

The load–strain curves of the steel angle (or the steel tube) were obtained by extracting the data from strain gauges, as shown in Figure 7. In the figures,  $\epsilon_h$  represents the transverse strain,  $\epsilon_v$  represents the vertical strain,  $\epsilon_e$  represents the equivalent elastic strain, and  $\epsilon_y$  means the yield strain. The steel angle and steel tube could be considered to be in a bidirectional plane stress state, as the extrusion pressures of concrete to the steel angle (or steel tube) are far less than the transverse and vertical stress of the steel angle (or steel tube). Assuming that the steel is an ideal elastoplastic material, and before the point at which the steel yields, the relationship of stress–strain can be written as Equation (1):

$$\begin{Bmatrix} \sigma_h \\ \sigma_v \end{Bmatrix} = \frac{E_s}{1 - \nu_s^2} \begin{bmatrix} 1 & \nu_s \\ \nu_s & 1 \end{bmatrix} \begin{Bmatrix} \epsilon_h \\ \epsilon_v \end{Bmatrix} \tag{1}$$

where  $\sigma_h$  and  $\sigma_v$  represent the transverse and vertical strain, respectively;  $E_s$  is the elastic modulus; and  $\nu_s$  is the Poisson’s ratio of steel, which is determined as 0.3.

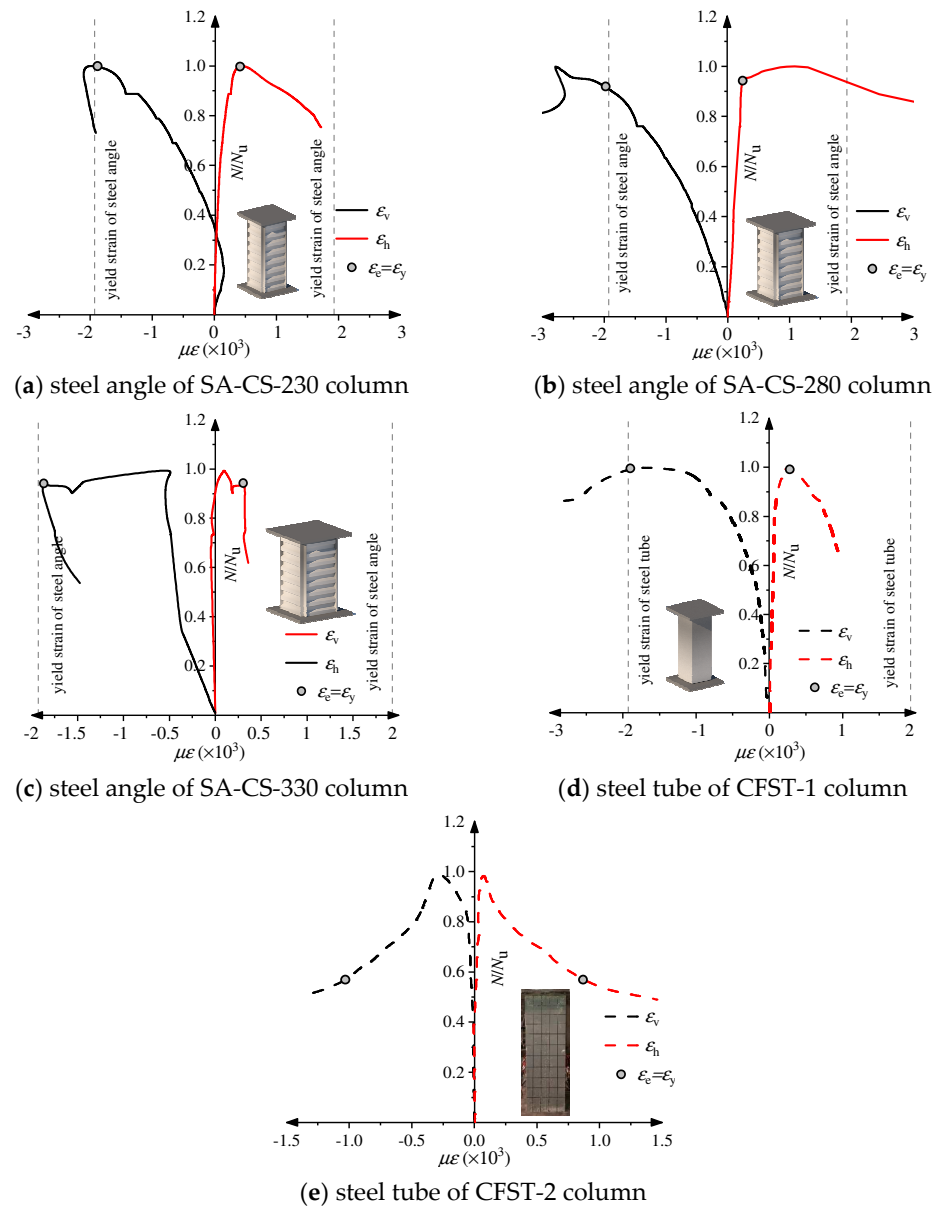


Figure 7. Load–strain curves.

Combined with the criterion proposed by Von Mises (Equation (2)) and Equation (1), the expression of the equivalent elastic strain could be obtained, which is shown in Equation (3) [26].

$$\sigma_e = \sqrt{\sigma_h^2 - \sigma_h \sigma_v + \sigma_v^2} \tag{2}$$

$$\varepsilon_e = \frac{\sigma_e}{E_s} = \frac{1}{1 - \nu_s^2} \sqrt{(1 - \nu_s + \nu_s^2)(\varepsilon_h^2 + \varepsilon_v^2) + (-1 + 4\nu_s - \nu_s^2)\varepsilon_h \varepsilon_v} \tag{3}$$

When  $\varepsilon_e = \varepsilon_y$ , the steel angle and steel tube are considered to yield. Compared with the transverse strain, the vertical strain of the steel angle and steel tube was much larger, which was close to the yield strain.

### 3.4. Strength Index of Core Concrete

In order to evaluate the improvement degree of the compressive strength of the core concrete in the different column types, the strength index ( $I_s$ ) of core concrete was adopted, which is defined as the strength of confined core concrete ( $f_{cc}$ ) normalized by the

prism compressive strength of concrete ( $f_c$ ) [27]. The strength index can be calculated as Equation (4):

$$I_s = A_c f_{cc} / A_c f_c = f_{cc} / f_c \tag{4}$$

where  $A_c$  is the area of core concrete.

As we were unable to measure the stress of the core concrete directly, the compressive strength of the core concrete was determined by separation analysis, which is a numerical analysis method. Calculating the stress of the steel angle and steel tube, the stress change of the core concrete was determined according to the balance condition. Combined with the load–strain curves of the specimens (Figure 7) and Equations (1)~(3), the stress state of the steel angle and steel tube can be determined under the ultimate bearing capacity ( $N_u$ ). The corrugated steel plates did not bear the axial load for the SA-CS columns, which was proven in previous studies [18,19]. Based on the principle of superposition,  $N_u$  can be written as Equation (5):

$$N_u = A_{s2} \sigma_{vu} + A_c f_{cc} \tag{5}$$

where  $A_{s2}$  is the area of the steel angle (for SA-CS column) or steel tube (for CFST column);  $\sigma_{vu}$  is the vertical stress of the steel angle (for SA-CS column) or steel tube (for CFST column) corresponding to the peak load.  $\sigma_{vu}$  is calculated from the vertical strain under peak load ( $\varepsilon_{vu}$ ) and the stress–strain relationship (Equation (1)). Judge the relationship between  $\varepsilon_{vu}$  and the vertical component of equivalent elastic strain ( $\varepsilon_{ve}$ ). If  $\varepsilon_{vu} \geq \varepsilon_{ve}$ , the value of  $\varepsilon_{ve}$  is taken as the value of  $\varepsilon_{vu}$ . If  $\varepsilon_{vu} < \varepsilon_{ve}$ , the value of  $\varepsilon_{vu}$  is taken as the actual value. The calculated results have some deviations but are within the acceptable range.

Thus, the strength of confined core concrete can be calculated by:  $f_{cc} = (N_u - A_{s2} \sigma_{vu}) / A_c$ .

Figure 8 illustrates the strength index  $I_s$  of the core concrete in the different specimens. For all the samples, the  $I_s$  was larger than 1.0, indicating that a steel skeleton (made of steel angles and corrugated steel plates) and steel tubes can provide confinement to core concrete. However, the  $I_s$  of the SA-CS-230 column was 17.84% greater than that of the CFST-1 column and 12.29% greater than that of the CFST-2 column at a similar steel ratio ( $\alpha$ ). The results presented that the steel skeleton (made of steel angles and corrugated steel plates) confined the core concrete more effectively than the steel tube. For the SA-CS columns, the  $I_s$  decreased with the decline of the steel ratio, but the degree was very slight. It is speculated that the reason for this phenomenon is that the transverse stress of the corrugated steel plates of all the specimens did not reach the yield strength under the peak load, which provided sufficient confinement for the core concrete. On the other hand, with the increase in the section size, the ratio of the size of the steel angle to the section size gradually decreases, and the shape of the core concrete tends to be more regular, which is conducive to reducing the arch effect. In conclusion, the sensitivity of  $I_s$  to the steel ratio is low.

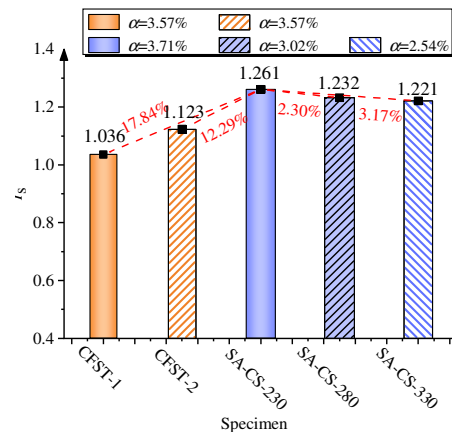


Figure 8. Strength index of core concrete.



### 3.5. Ductility Index of Specimens

The ductility index ( $\mu$ ) can reflect the deformation properties of the specimens, whose calculation method is the ratio of  $\Delta_{u-0.85}$  to  $\Delta_y$ , as shown in Equation (6):

$$\mu = \Delta_{u-0.85} / \Delta_y \tag{6}$$

where  $\Delta_{u-0.85}$  is the displacement corresponding to the load dropping to 85% peak load ( $0.85N_u$ );  $\Delta_y$  is the displacement corresponding to the yield load, which is determined by the equivalent elastic-plastic energy method [28]. In the equivalent elastic-plastic energy method, the original curve is replaced with an ideal elastic-plastic line with the same envelope area and concerning the displacement of the inflection point of the line as the yield point. Figure 9 shows the method of determining  $\Delta_{u-0.85}$  and  $\Delta_y$ .

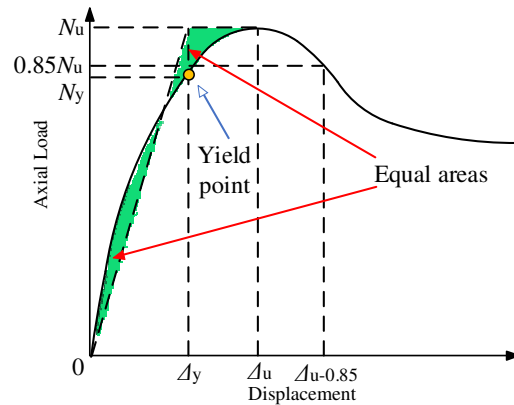


Figure 9. Equivalent elastic-plastic energy method.

Figure 10 plots the ductility index  $\mu$  of the different specimens. Compared with the SA-CS-230 column, the  $\mu$  of the CFST-1 column decreased by 22.36%, while the  $\mu$  of the CFST-2 column decreased by 16.67%. Combined with the results of  $I_s$ , it can be inferred that the mechanical properties of the SA-CS column are better than those of the CFST column. In addition, for the SA-CS columns, the ductility index presented a downward trend with the increase in the section size, which might have occurred because as the section size of the specimen increases, the transverse stress of the corrugated steel plate increases. The corrugated steel plates would yield earlier, which leads to the specimen presenting a steeper slope in the descending stage, resulting in a decrease in  $\Delta_{u-0.85}$ .

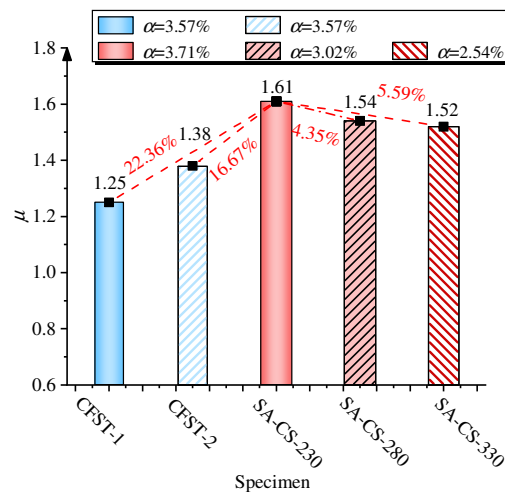


Figure 10. Ductility index of specimens.

However, like  $I_s$ , the  $\mu$  also decreased slightly with the decline of the steel ratio. The phenomenon indicated that the mechanical properties of the SA-CS column are slightly affected by the steel ratio. This phenomenon can be considered to reduce the steel ratio appropriately for the new type of composite column in the project.

#### 4. Finite Element Analysis

In the study, the samples of the experiment were limited, and the only variable was the section size. To further study the axial compression behavior of the SA-CS column under different parameters, the nonlinear finite element program ABAQUS was adopted to establish the models.

##### 4.1. Model Set-Up

The solid mesh of three-dimensional structural eight-node brick elements with reduced integration (C3D8R) was adopted for all the model parts, including the core concrete, corrugated steel plates, and steel angles. The mesh size would influence the accuracy of the calculation. Combined with the calculation cost, the mesh division method was selected with 10 mm as the minimum control size.

The steel angle and the corrugated steel plate were connected by a “Tie” to simulate the welding mode. The interaction between the core concrete and steel (including the steel angle and corrugated steel plate) adopted the “surface-to-surface” contact method, whose normal direction was defined as hard contact, while tangential direction was defined as friction contact. The friction coefficient of 0.6 coincided better with the test results and the Refs. [5,22,29] also employed the same friction coefficient.

Reference point 1 was coupled at the top part of the model with a vertical loaded displacement of 10 mm. Reference point 2 was coupled at the bottom part of the model, set as a rigid connection (all directions were constrained). Consider and apply the residual stress at the joint between the corrugated steel plate and steel angle to simulate the welds. Denote the residual stress as  $0.2 f_y$  [10], where  $\sigma_{rt}$  represents the tensile residual stress, and  $\sigma_{ct}$  represents the compressive residual stress. The details of the model are illustrated in Figure 11.

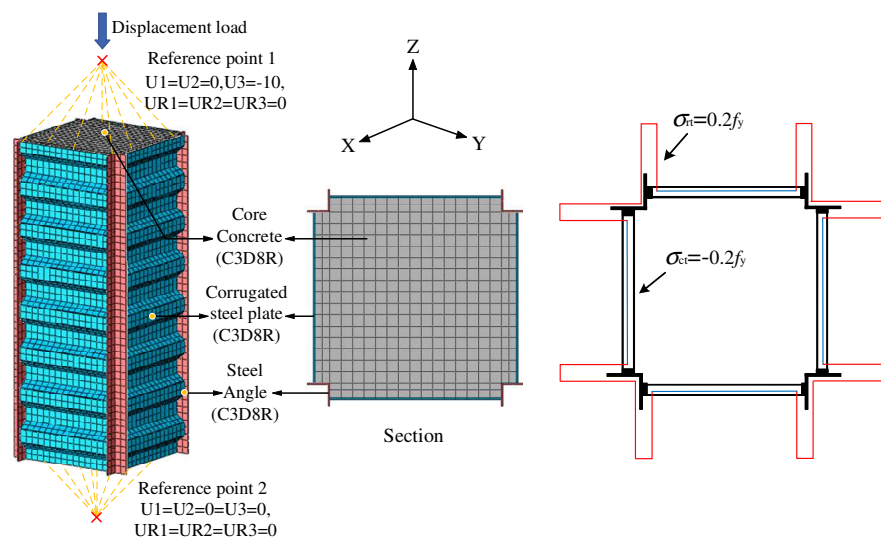


Figure 11. FE model of SA-CS column.

##### 4.2. Material Models

###### (1) Core concrete

The concrete damage plasticity (CDP) model was used to simulate the plastic behavior of concrete for its high accuracy. The Poisson’s ratio of core concrete was taken as 0.2, and the initial Young’s modulus of core concrete was calculated as  $4700 f_c^{0.5}$  [30]. The viscosity

parameter was 0.0005. The invariable stress ratio ( $K_c$ ) and the ratio of the initial equiaxial compressive yield stress to the initial uniaxial compressive yield stress ( $f_{bo}/f_{co}$ ) was needed to define the yield surface function [31]. In order to calculate the plastic flow potential of concrete, it was necessary to determine the dilation angle ( $\psi$ ) and the flow potential eccentricity ( $e$ ). The values of  $\psi, e, f_{bo}/f_{co}$ , and  $K_c$  were  $35^\circ, 0.1, 1.16$ , and  $0.667$ , respectively.

The constitutive relationship of confined concrete suggested by Han [32] et al. was adopted as the compressed stress–strain relationship for the core concrete, as given in Equations (7)–(13). In addition, to determine the tensile behavior of concrete, we adopted the simplified model proposed by Liu [33].

$$y = \begin{cases} 2x - x^2 & (0 \leq x \leq 1) \\ \frac{x}{\beta_o(x-1)^\eta + x} & (x > 1) \end{cases} \tag{7}$$

$$x = \varepsilon/\varepsilon_o \tag{8}$$

$$y = \sigma/\sigma_o \tag{9}$$

$$\sigma_o = f'_c \tag{10}$$

$$\varepsilon_o = (800\zeta^{0.2} + 1300 + 12.5f'_c) \times 10^{-6} \tag{11}$$

$$\beta_o = \frac{(f'_c)^{0.1}}{1.2\sqrt{1 + \zeta}} \tag{12}$$

$$\eta = 1.6 + 1.5/x \tag{13}$$

where  $\beta_o$  is the adjusting parameter of the stress–strain curve of the descending section of compressive concrete;  $\eta$  is the curve shape coefficient;  $\varepsilon$  and  $\sigma$  are the strain and corresponding stress of concrete;  $\varepsilon_o$  and  $\sigma_o$  are the peak strain and corresponding stress of concrete;  $f'_c$  is the cylinder compressive strength of concrete, which is calculated as  $0.8f_{cu}$ ; and  $\zeta$  is the confinement index, which is calculated as  $f_{y1}A_{s1}/f_cA_c$ , where  $A_{s1}$  is the area of the corrugated steel plate.

(2) Steel

As the constitutive steel model has little influence on the bearing capacity of a steel–concrete composite column [34], this research adopts the ideal elastic–plastic model to describe the stress–strain relationship of steel to simplify the calculations [35]. Both the elastic modulus and the yield strength of the steel used measured values, and the Poisson’s ratio of steel was taken as 0.3. The model was described as follows:

$$\sigma_s = \begin{cases} E_s\varepsilon_s & (\varepsilon_s \leq \varepsilon_y) \\ f_y + E_p(\varepsilon_s - \varepsilon_y) & (\varepsilon_s > \varepsilon_y) \end{cases} \tag{14}$$

where  $\varepsilon_s$  and  $\sigma_s$  are the strain and stress of steel, and  $E_p$  is taken as  $0.01E_s$ .

4.3. Model Validation

The experimental and numerical results regarding the failure modes, load–displacement curves, ultimate bearing capacity, and corresponding displacement were compared to validate the accuracy of the FE model. The SA-CS-280 column was taken as an example, whose failure modes are shown in Figure 12. The local buckling of the steel angle and the conquassation of the core concrete were highly consistent. Figure 13a–c illustrates the comparison of the load–displacement curves between the test and FE simulation, which were in good agreement. The deviation of the ultimate bearing capacity and the corresponding displacement was within 10%. Overall, the FE model established in this paper could simulate the mechanical properties of the SA-CS column with reasonable precision. In addition, using the FE model to analyze different parameters was reasonable and reliable.

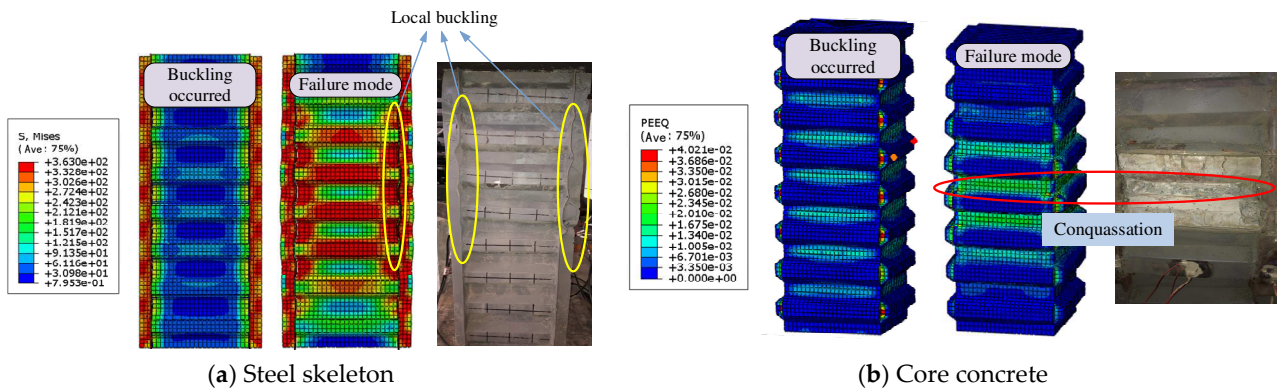


Figure 12. Comparison between test and FE.

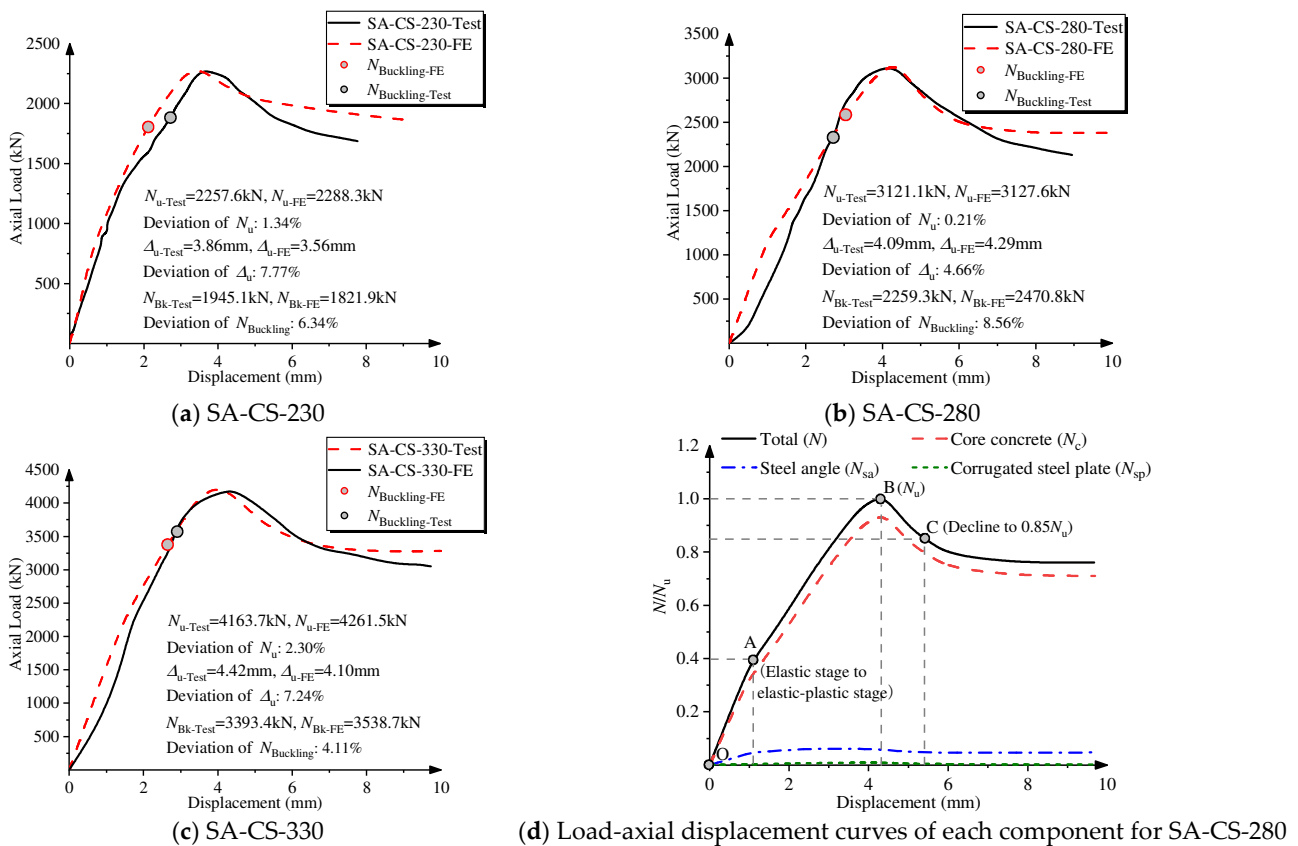


Figure 13. Comparison of FE and test load–axial displacement curves.

Figure 13d plots the  $N/N_u$ -displacement curves of each component of the SA-CS-280 column. During the loading process, the core concrete bore most of the load—more than 90% of the total. In addition, the corrugated steel plate did not bear the load, which proved the opinion presented in Section 3.4.

#### 4.4. Parametric Analysis

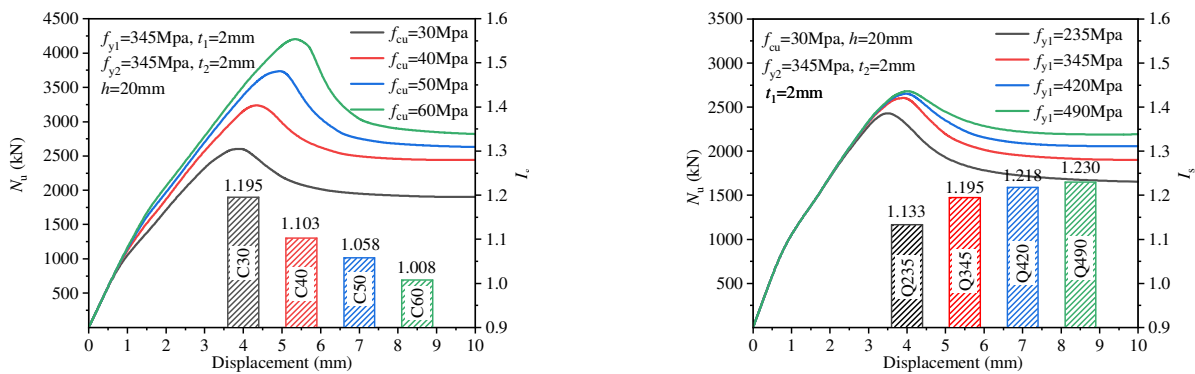
In order to evaluate the influence of different parameters on the axial compressive behavior of the SA-CS column, a parametric analysis was carried out based on the validated model. The variation included the compressive strength of concrete ( $f_{cu}$ ), the yield strength ( $f_{y1}$ ) and thickness ( $t_1$ ) of the corrugated steel plate, the yield strength ( $f_{y2}$ ) and thickness ( $t_2$ ) of the steel angle, and the wave height of the corrugated steel plate ( $h$ ). The values of the parameters are listed in Table 2. To ensure the use of a single variable in the parametric analysis, the width of all FE models was 280 mm.

**Table 2.** Parameters of FE model.

Parameters	Symbols and Units	Values
Compressive strength of concrete	$f_{cu}$ (MPa)	30, 40, 50, 60
Yield strength of corrugated steel plate	$f_{y1}$ (MPa)	235, 345, 420, 490
Thickness of corrugated steel plate	$t_1$ (mm)	1, 2, 3, 4
Yield strength of steel angle	$f_{y2}$ (MPa)	235, 345, 420, 490
Thickness of steel angle	$t_2$ (mm)	1, 2, 3, 4
Wave height of corrugated steel plate	$h$ (mm)	15, 20, 25, 30

Figure 14 illustrates the influence of the parameters on the load–displacement curves of the specimens and the core concrete’s strength index ( $I_s$ ). Figure 14a shows that the ultimate bearing capacity ( $N_u$ ) increased with the improvement of  $f_{cu}$ . Still, the results regarding  $I_s$  and ductility were opposite, indicating that the confinement effect of the core concrete provided by the outer steel skeleton decreased. Especially when  $f_{cu}$  was taken as 60 MPa,  $I_s$  was just 1.008 and the core concrete was unconfined. Figure 14b,c show that  $N_u$ ,  $\mu$ , and  $I_s$  increased with the improvement of  $f_{y1}$  or  $t_1$ , which demonstrated that the corrugated steel plate served primarily to confine the core concrete. In addition, with respect to Figure 14d,e, the general shapes of the load–displacement curves, including the initial stiffness and softening region, were similar.  $N_u$  and  $I_s$  were not obviously affected by the improvement of  $f_{y2}$  or  $t_2$ . It can be inferred that the steel angle had little effect on confining concrete and only played a role in bearing the load. Figure 14f shows the influence of  $h$  on the load–displacement curves and  $I_s$ .  $N_u$  increased with the improvement of  $h$ , but for  $I_s$ , the variation trend was not monotonous: it increased first and then decreased. In order to explore the wave heights that could provide the most effective confinement of core concrete, the wave heights between 25 mm and 30 mm were divided in detail, and an FE simulation was carried out. The results are shown in Figure 15. It can be seen from the figure that when  $h = 24$  mm, the value of  $I_s$  was the maximum.

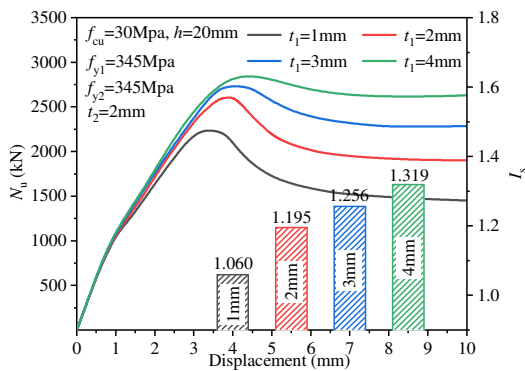
A total of 23 FE models were established in this section. To conveniently distinguish them, the FE models were named SA-CS-1~SA-CS-23. The design parameters, material properties, and numerical results of the FE models, including the models corresponding to SA-CS-230, SA-CS-280, and SA-CS-330, are listed in Table 3.



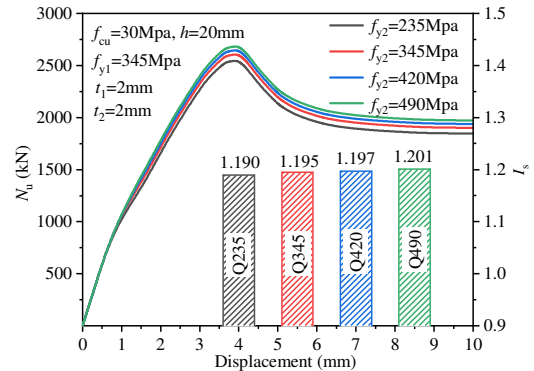
(a) Influence of compressive strength of concrete. (b) Influence of yield strength of corrugated steel plate.

**Figure 14.** Cont.

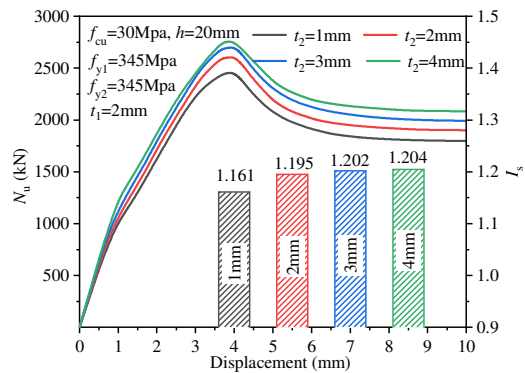




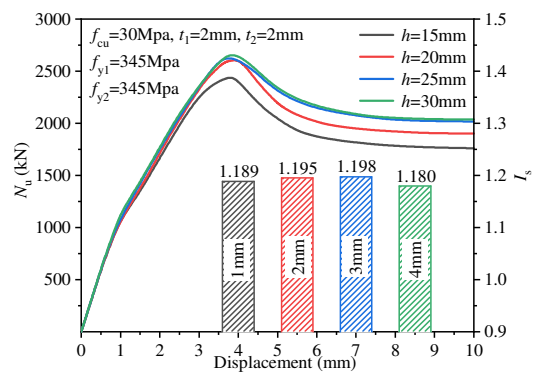
(c) Influence of thickness of corrugated steel plate.



(d) Influence of yield strength of steel angle.



(e) Influence of thickness of steel angle.



(f) Influence of wave height of corrugated steel plate.

Figure 14. Results of FE parametric analysis.

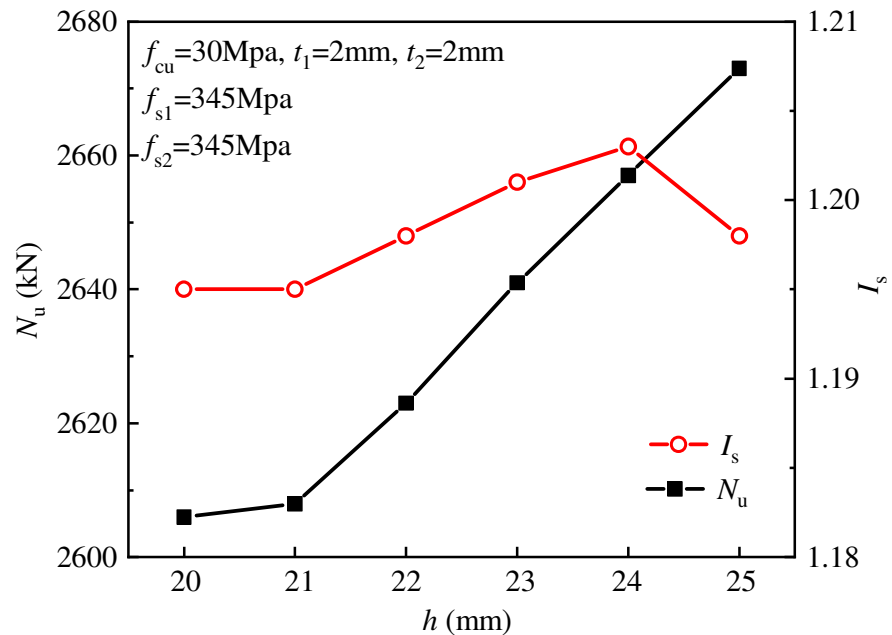


Figure 15. Influence of wave height of corrugated steel plate on Nu and Is.

**Table 3.** Specific parameters and results of models.

Specimen Designation	B/mm	$t_1$ /mm	$t_2$ /mm	$f_{cu}$ /MPa	$f_{y1}$ /MPa	$f_{y2}$ /MPa	h/mm	$I_s$	$N_{u-FEM}$ /kN
SA-CS-1	280	2	2	30	325	325	20	1.195	2606.1
SA-CS-2	280	2	2	40	325	325	20	1.103	3253.7
SA-CS-3	280	2	2	50	325	325	20	1.058	3740.8
SA-CS-4	280	2	2	60	325	325	20	1.008	4215.7
SA-CS-5	280	2	2	30	235	325	20	1.133	2476.3
SA-CS-6	280	2	2	30	420	325	20	1.218	2654.7
SA-CS-7	280	2	2	30	490	325	20	1.230	2681.8
SA-CS-8	280	2	2	30	325	235	20	1.190	2545.0
SA-CS-9	280	2	2	30	325	420	20	1.197	2646.4
SA-CS-10	280	2	2	30	325	490	20	1.201	2683.4
SA-CS-11	280	1	2	30	325	325	20	1.060	2252.6
SA-CS-12	280	3	2	30	325	325	20	1.256	2743.9
SA-CS-13	280	4	2	30	325	325	20	1.319	2875.2
SA-CS-14	280	2	1	30	325	325	20	1.161	2454.4
SA-CS-15	280	2	3	30	325	325	20	1.202	2699.5
SA-CS-16	280	2	4	30	325	325	20	1.204	2761.3
SA-CS-17	280	2	2	30	325	325	15	1.189	2448.6
SA-CS-18	280	2	2	30	325	325	21	1.195	2605.1
SA-CS-19	280	2	2	30	325	325	22	1.198	2623.9
SA-CS-20	280	2	2	30	325	325	23	1.202	2641.6
SA-CS-21	280	2	2	30	325	325	24	1.203	2657.0
SA-CS-22	280	2	2	30	325	325	25	1.198	2672.8
SA-CS-23	280	2	2	30	325	325	30	1.180	2688.4
SA-CS-230	230	2	2	35.4	324	324	20	1.261	2288.3
SA-CS-280	280	2	2	35.4	324	324	20	1.232	3127.6
SA-CS-330	330	2	2	35.4	324	324	20	1.221	4261.5

## 5. Ultimate Bearing Capacity

### 5.1. Comparison with the Existing Codes

In order to study the applicability of the existing codes to the ultimate bearing capacity of the SA-CS column, we conducted a comparison between the FE-simulated results and the calculation results according to the existing codes of GB50936-2014 [36], Eurocode 4-2004 [37], ACI 318-14 [30], DBJ/T13-51-2010 [38], and AIJ-2001 [39]. Table 4 lists the results.

**Table 4.** Comparison of ultimate bearing capacity between FE results and design codes.

Specimen Designation	GB50936-2014		Eurocode 4-2004		ACI 318-14		DBJ/T13-51-2010		AIJ-2001	
	$N_{u-Cal}$	$N_{u-FEM}/N_{u-Cal}$	$N_{u-Cal}$	$N_{u-FEM}/N_{u-Cal}$	$N_{u-Cal}$	$N_{u-FEM}/N_{u-Cal}$	$N_{u-Cal}$	$N_{u-FEM}/N_{u-Cal}$	$N_{u-Cal}$	$N_{u-FEM}/N_{u-Cal}$
SA-CS-1	3201.6	0.814	2191.7	1.189	1885.5	1.382	3197.2	0.815	1926.2	1.353
SA-CS-2	4026.9	0.808	2871.9	1.133	2463.8	1.321	4005.5	0.812	2504.5	1.299
SA-CS-3	4858.2	0.770	3164.7	1.182	2712.6	1.379	4813.9	0.777	2753.3	1.359
SA-CS-4	5681.5	0.742	4232.5	0.996	3620.3	1.164	5622.3	0.750	3661.0	1.152
SA-CS-5	2987.1	0.829	2191.7	1.130	1885.5	1.313	3020.5	0.820	1926.2	1.286
SA-CS-6	3447.7	0.770	2191.7	1.211	1885.5	1.408	3383.6	0.785	1926.2	1.378
SA-CS-7	3638.8	0.737	2191.7	1.224	1885.5	1.422	3521.0	0.762	1926.2	1.392
SA-CS-8	3189.2	0.798	2149.9	1.184	1843.8	1.380	3160.0	0.805	1873.2	1.359
SA-CS-9	3211.7	0.824	2235.7	1.184	1929.6	1.371	3236.3	0.818	1982.2	1.335
SA-CS-10	3221.4	0.833	2268.2	1.183	1962.1	1.368	3265.2	0.822	2023.5	1.326
SA-CS-11	2869.6	0.785	2219.6	1.015	1909.3	1.180	2809.3	0.802	1855.9	1.214
SA-CS-12	3522.3	0.779	2163.9	1.268	1861.9	1.474	3588.6	0.765	1993.4	1.376
SA-CS-13	3838.7	0.749	2136.3	1.346	1838.5	1.564	3983.7	0.722	2057.5	1.397
SA-CS-14	3191.7	0.769	2130.6	1.152	1822.5	1.347	3184.2	0.771	1937.4	1.267

Table 4. Cont.

Specimen Designation	GB50936-2014		Eurocode 4-2004		ACI 318-14		DBJ/T13-51-2010		AIJ-2001	
	$N_{u-Cal}$	$N_{u-FEM}/N_{u-Cal}$	$N_{u-Cal}$	$N_{u-FEM}/N_{u-Cal}$	$N_{u-Cal}$	$N_{u-FEM}/N_{u-Cal}$	$N_{u-Cal}$	$N_{u-FEM}/N_{u-Cal}$	$N_{u-Cal}$	$N_{u-FEM}/N_{u-Cal}$
SA-CS-15	3206.1	0.842	2250.1	1.200	1945.9	1.387	3210.0	0.841	1915.1	1.410
SA-CS-16	3210.8	0.860	2305.9	1.197	2003.7	1.378	3222.6	0.857	1904.0	1.450
SA-CS-17	3111.3	0.787	2126.2	1.152	1829.9	1.338	3122.5	0.784	1870.6	1.309
SA-CS-18	3216.2	0.810	2204.7	1.182	1896.6	1.374	3212.1	0.811	1937.4	1.345
SA-CS-19	3235.4	0.811	2217.8	1.183	1907.8	1.375	3227.0	0.813	1948.5	1.347
SA-CS-20	3253.2	0.812	2230.9	1.184	1918.9	1.377	3242.0	0.815	1959.6	1.348
SA-CS-21	3272.2	0.812	2244.0	1.184	1930.0	1.377	3256.9	0.816	1970.7	1.348
SA-CS-22	3287.6	0.813	2257.1	1.184	1941.1	1.377	3271.8	0.817	1981.8	1.349
SA-CS-23	3377.4	0.796	2322.5	1.158	1996.7	1.346	3346.5	0.803	2037.4	1.319
SA-CS-230	2627.2	0.871	1806.3	1.267	1557.9	1.469	2649.0	0.864	1598.5	1.432
SA-CS-280	3645.2	0.858	2558.5	1.222	2197.3	1.423	3631.3	0.861	2237.9	1.398
SA-CS-330	4820.7	0.884	3450.7	1.235	2955.6	1.442	4773.0	0.893	2996.2	1.422
Mean value		0.806		1.183		1.374		0.808		1.345
Standard deviation		0.038		0.068		0.078		0.037		0.064

### 5.1.1. GB50936-2014

The calculation principle of GB50936-2014 is a unified theory that regards concrete and steel as a unity. The confinement index  $\zeta$  is introduced to describe the confined effect between concrete and steel. The ultimate bearing capacity of the SA-CS column can be calculated as in the following Equations.

$$N_{u-GB} = \varphi N_{sc} = \varphi A_c f_{sc} \quad (15)$$

$$f_{sc} = (1.212 + B\zeta + C\zeta^2) f_c \quad (16)$$

$$B = \frac{0.131 f_{y1}}{213} + 0.723 \quad (17)$$

$$C = \frac{-0.07 f_c}{14.4} + 0.026 \quad (18)$$

where  $\varphi$  is the stability coefficient under axial compression, whose value is 1.0;  $f_{sc}$  is the compressive strength of the unity.

The mean value of the ratio of the simulated results to calculated results ( $N_{u-FEM}/N_{u-Cal}$ ) is 0.806, and the standard deviation is 0.038. The estimated results of the ultimate bearing capacity have poor dispersion, and the calculated value is too large. In GB50936-2014, limits are specified for the width-to-thickness ratio ( $B/t$ ) of square CFST, which should not be greater than  $60\sqrt{235/f_{y1}}$ . However, the  $B/t$  of experimental specimens and numerical models both exceed the limit, which might be the reason for the deviation between the calculated and actual results.

### 5.1.2. Eurocode 4-2004

According to Eurocode 4-2004, the core concrete is not considered to be confined by the steel tube, and the ultimate bearing capacity of the SA-CS column can be obtained by Equation (19).

$$N_{u-EC4} = f'_c A_c + f_{y2} A_{s2} \quad (19)$$

The mean value of  $N_{u-FEM}/N_{u-Cal}$  is 1.183, and the standard deviation is 0.068. The calculated results corresponding to the ultimate bearing capacity are low and safe.

### 5.1.3. ACI 318-14

Similar to Eurocode 4-2004, ACI 318-14 also does not consider the confinement of core concrete, whose compressive strength is even reduced by 15%. The calculation method is shown in Equation (20).

$$N_{u-ACI} = 0.85 f'_c A_c + f_{y2} A_{s2} \quad (20)$$

The mean value of  $N_{u-FEM}/N_{u-Cal}$  is 1.374, and the standard deviation is 0.078. The calculated results have strong dispersion. In Eurocode 4-2004 and ACI 318-14, the confinement

effect on the core concrete is ignored, and the bearing capacity is the simple superposition of the concrete and steel angle. It is undoubtable that the calculation results are smaller than the actual results.

#### 5.1.4. DBJ/T13-51-2010

The calculated method of DBJ13-51-2010 is similar to GB50936-2014, which is based on the unified theory and introduces the confined index  $\zeta$  and stability coefficient  $\varphi$ . The ultimate bearing capacity can be calculated as follows:

$$N_{u-DB} = \varphi N_{sc} = \varphi A_c f_{sc} \quad (21)$$

$$f_{sc} = (1.18 + 0.85\zeta)f_c \quad (22)$$

The mean value of  $N_{u-FEM}/N_{u-Cal}$  is 0.808, and the standard deviation is 0.037—basically the same as the results calculated by GB50936-2014. The reason for the departure of the calculation results is consistent with GB50936-2014.

#### 5.1.5. AIJ-2001

AIJ-2001 considers the strength enhancement of composite columns by defining a lifting coefficient  $\eta$  for the bearing capacity of steel.  $\eta$  is taken as 0.27, and Equation (23) shows the calculation method.

$$N_{u-AIJ} = 0.85f'_c A_c + (1 + \eta)f_{s2} A_{s2} \quad (23)$$

where  $f_{s2}$  is taken from the smaller values in  $f_{y2}$  and  $0.7f_{u2}$ , and  $f_{u2}$  is the tensile strength of the steel angle.

The mean value of  $N_{u-FEM}/N_{u-Cal}$  is 1.345, and the standard deviation is 0.064. AIJ-2001 improves the bearing capacity of the steel angle but ignores the confinement effect on the core concrete. For the SA-CS columns, the primary function of the steel angles is to connect with the corrugated steel plates, and the core concrete bears more than 90% of the load. Thus, the calculation results are smaller than the actual results.

Overall, the results show that the existing codes could not calculate the ultimate bearing capacity of the SA-CS column accurately. The codes always underrate or overrate the experimental and numerical results.

### 5.2. Proposed Design Model

According to the principle of superposition, the ultimate bearing capacity of the SA-CS column could be calculated as Equation (24). In addition, early investigations presented that the compressive strength of confined concrete, which is under triaxial stress, is related to the effective confining stress ( $f_r$ ), which can be expressed by Equation (25) [40].

$$N_u = f_{cc} A_c + f_{y2} A_{s2} \quad (24)$$

$$f_{cc} = f_c + 5.3f_r \quad (25)$$

As the cross-section of the SA-CS column is similar to a square, the arch effect exists in the column, which leads to only a portion of the core concrete being effectively confined. The core concrete is divided into the effectively confined area ( $A_{ec}$ ) and the ineffectively confined area ( $A_{ic}$ ). Figure 16 shows the division method. The effective confining coefficient ( $k_e$ ) is determined as the ratio of the effective confined area to the total area and the calculated formulation is expressed as Equations (26) and (27).

$$A_c = B^2 + 2B(h - t_2) \quad (26)$$

$$k_e = \frac{A_{ec}}{A_c} = \frac{A_c - 4A_{ic}}{A_c} = 1 - \frac{(\frac{\pi}{2} - 1)B}{B + 2(h - t_2)} \quad (27)$$

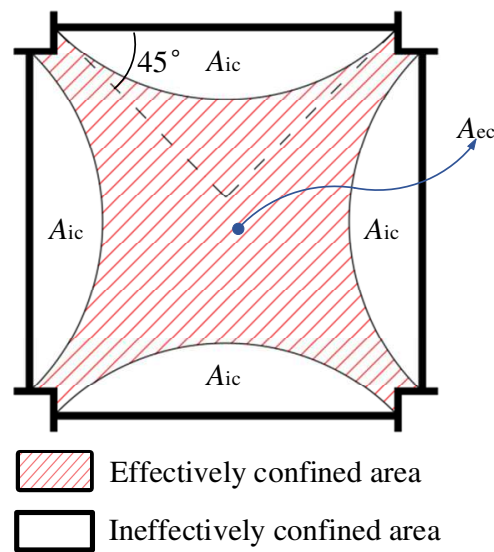


Figure 16. Division of effectively and ineffectively areas.

Based on the principle of the equal area of materials, the section of the SA-CS column can be converted to a square section, as shown in Figure 17. Equation (28) expresses the relationship between  $f_r$  and the transverse stress ( $\sigma_{sh}$ ) according to the force equilibrium [41]:

$$f_r = \frac{2k_e t' \sigma_{sh}}{B' - 2t'} \tag{28}$$

where  $B'$  is the width of the equivalent square and can be calculated as  $B' = \sqrt{A_c + A_{s1}}$ ;  $t'$  is the thickness of the equivalent square and can be calculated as  $t' = (\sqrt{A_c + A_{s1}} - \sqrt{A_c}) / 2$ .

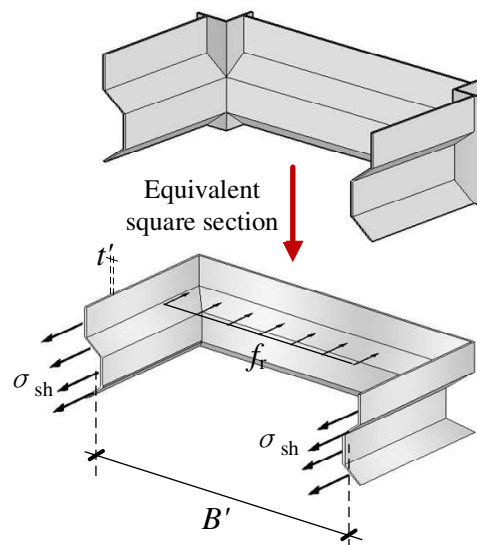


Figure 17. Equivalent conversion and force equilibrium.

Referring to the paper by Wang [19], the value of  $\sigma_{sh}$  can be calculated by Equation (29), and Figure 18 illustrates the calculation results of the proposed design model. Compared with the existing codes, the proposed model can achieve results that are in good agreement with the FE results, whose deviation is less than 10%.

$$\sigma_{sh} = 0.78e^{0.24 - 0.4\sqrt{\xi}} f_{y1} \tag{29}$$



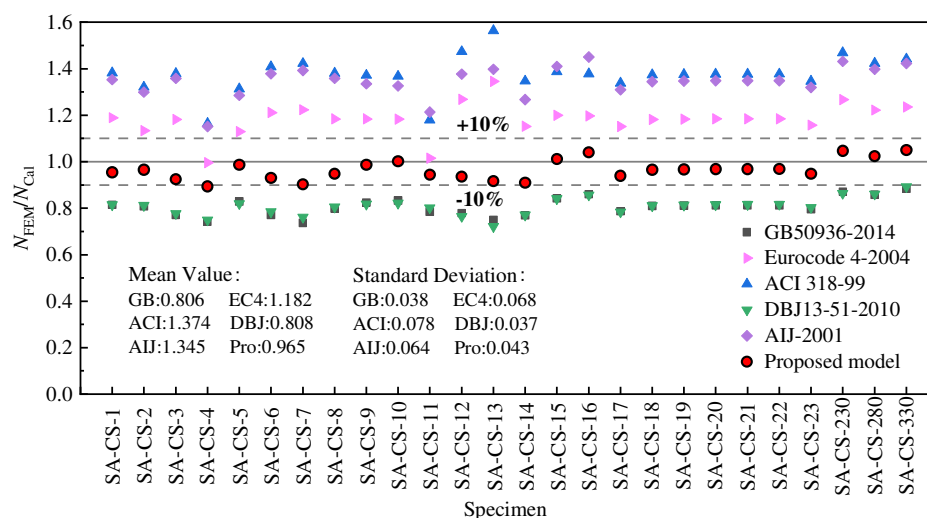


Figure 18. Comparison of  $N_{u-FEM}/N_{u-Cal}$  between existing codes and proposed design method.

### 6. Conclusions

Three SA-CS columns and one CFST column were tested under axial compression and compared with respect to their mechanical behavior. The FE model of the SA-CS column was established, and a parametric analysis was conducted. The calculation methods of some existing codes were assessed by comparing the calculated and numerical results and proposing a new calculation method for the SA-CS column. The results demonstrated herein show that:

- (1) All the SA-CS columns failed with the severe local buckling of the steel angle and the spalling of the crest of the core concrete. The CFST column failed with the steel tube’s buckling and the internal concrete’s shear failure. The strength index ( $I_s$ ) and ductility index ( $\mu$ ) of the SA-CS column were better than those of the CFST column with a similar steel ratio, indicating that the SA-CS column provided more excellent confinement effects on the core concrete than the CFST column.
- (2) The increase in the section width (decrease of the steel ratio) of the SA-CS column improved the ultimate bearing capacity but reduced  $I_s$  and  $\mu$ . However, the degree of decline of  $I_s$  and  $\mu$  was slight, indicating that the SA-CS column’s mechanical properties were only slightly affected by the steel ratio in a particular range. In practical engineering, reducing the steel ratio of the SA-CS column can be considered to improve economic benefits.
- (3) The FE models were in good agreement with the experimental results. The parametric analysis results have shown that the corrugated steel plate primarily confined the core concrete, and the steel angle bore a part of the axial load.
- (4) Increasing the compression strength of concrete can effectively improve the ultimate bearing capacity of the specimens but  $I_s$  and  $\mu$  will decrease. Increasing the yield strength and thickness of the corrugated steel plate will improve the confinement effect on the core concrete to enhance the axial compression behavior of the specimen. The yield strength and the thickness of the steel angle had little influence on the mechanical properties of the specimens. The variation trend of  $I_s$  was not monotonous with the increase in the wave height of the corrugated steel plate ( $h$ ), and the confinement of the corrugated steel plate to the core concrete was the strongest when  $h$  was taken as 24 mm.
- (5) A comparison of the ultimate bearing capacities between the FE results and calculated results by some current codes was conducted, and it was found that the existing codes always underrated or overrated the ultimate bearing capacity of the SA-CS column. The fundamental reason is that the current codes cannot accurately calculate the effective confining stress on the core concrete provided by the corrugated steel

plate. Thus, a new design model for the SA-CS column was proposed, which provided reasonably good predictions with FE-simulated results.

**Author Contributions:** Conceptualization, Y.Z.; data curation, Z.S.; formal analysis, Z.S.; funding acquisition, Y.Z.; investigation, L.W.; methodology, C.W.; project administration, Y.Z.; software, Z.S.; supervision, C.W.; validation, J.P.; visualization, Z.S.; writing-original draft, Z.S.; writing-review and editing, Z.S. All authors have read and agreed to the published version of the manuscript.

**Funding:** This research was supported by Jiangsu Province Department of Science and Technology (BE2018625) and National Natural Science Foundation of China (51873240). The financial supports are gratefully acknowledged.

**Institutional Review Board Statement:** Not applicable.

**Informed Consent Statement:** Not applicable.

**Data Availability Statement:** All data, models, or codes that support the findings of this study are available from the corresponding author upon reasonable request.

**Conflicts of Interest:** The authors declare that they have no conflict of interest regarding this work, the work described is original research that has not been published previously, and that it is not under consideration for publication elsewhere, in whole or in part.

## References

1. EN 1994-1-1; Eurocode 4. Design of Composite Steel and Concrete Structures. European Committee for Standardization: Brussels, Belgium, 2004.
2. DBJ/T13-2010; Technical Specification for Concrete-Filled Steel Tubular Structures. The Department of Housing and Urban-Rural Development of Fujian Province: Fuzhou, China, 2010.
3. GB 50936-2014; Technical Code for Concrete Filled Steel Tubular Structures. Chinese National Standards: Beijing, China, 2014.
4. ISO 6892-1:2019; Metallic Materials-Tensile Testing, Part 1: Method of Test at Room Temperature. Standards Press of China: Beijing, China, 2010.
5. GB 50010-2002; Code for Design of Concrete Structures. Ministry of Housing and UrbanRural Development of the People's Republic of China: Beijing, China, 2010.
6. Afaghi-Darabi, A.; Abdollahzadeh, G. Effect of cooling rate on the post-fire behavior of CFST column. *Comput. Concr.* **2019**, *23*, 281–294.
7. AIJ Standards for Structural Calculation of Steel Reinforced Concrete Structures; Architectural Institute of Japan: Tokyo, Japan, 2001.
8. Candappa, D.C.; Sanjayan, J.G.; Setunge, S. Complete triaxial stress-strain curves of high-strength concrete. *J. Mater. Civ. Eng.* **2001**, *13*, 209–215. [[CrossRef](#)]
9. Che, Y.; Wang, Q.L.; Shao, Y.B. Compressive performances of the concrete filled circular cfrp-steel tube (C-CFRP-CFST). *Adv. Steel Constr.* **2012**, *8*, 331–358.
10. Chen, J.; Chan, T.-M.; Chung, K.-F. Design of square and rectangular CFST cross-sectional capacities in compression. *J. Constr. Steel Res.* **2021**, *176*, 106419. [[CrossRef](#)]
11. Chen, Z.; Xu, R.; Ning, F.; Liang, Y. Compression behaviour and bearing capacity calculation of concrete filled double skin square steel columns. *J. Build. Eng.* **2021**, *42*, 103022. [[CrossRef](#)]
12. Chen, Z.; Zhou, J.; Jing, C.; Tan, Q. Mechanical behavior of spiral stirrup reinforced concrete filled square steel tubular columns under compression. *Eng. Struct.* **2021**, *226*, 111377. [[CrossRef](#)]
13. ACI 318-14; Building Code Requirements for Structural Concrete and Commentary. American Concrete Institute: Farmington Hills, MI, USA, 2011.
14. Ding, F.; Ying, X.; Zhou, L.; Yu, Z. Unified calculation method and its application in determining the uniaxial mechanical properties of concrete. *Front. Archit. Civ. Eng. China* **2011**, *5*, 381. [[CrossRef](#)]
15. Fang, Y.; Wang, Y.; Hou, C.; Lu, B. CFDST stub columns with galvanized corrugated steel tubes: Concept and axial behaviour. *Thin Wall Struct* **2020**, *157*, 107116. [[CrossRef](#)]
16. Gan, D.; Zhou, Z.; Zhou, X.H. Axially Loaded Thin-Walled Square Concrete-Filled Steel Tubes Stiffened with Diagonal Binding Ribs. *ACI Struct. J.* **2019**, *116*, 265–280. [[CrossRef](#)]
17. Han, L.-H.; Li, W.; Bjorhovde, R. Developments and advanced applications of concrete-filled steel tubular (CFST) structures: Members. *J. Constr. Steel Res.* **2014**, *100*, 211–228. [[CrossRef](#)]
18. Han, L.-H.; Yao, G.-H.; Tao, Z. Performance of concrete-filled thin-walled steel tubes under pure torsion. *Thin Wall. Struct.* **2007**, *45*, 24–36. [[CrossRef](#)]
19. İpek, S.; Erdoğan, A.; Güneyisi, E.M. Compressive behavior of concrete-filled double skin steel tubular short columns with the elliptical hollow section. *J. Build. Eng.* **2021**, *38*, 102200. [[CrossRef](#)]

20. Liu, J.; Zhou, X.; Dan, G. Effect of friction on axially loaded stub circular tubed columns. *Adv. Struct. Eng.* **2016**, *19*, 546–559. [[CrossRef](#)]
21. Kharoob, O.F.; Ghazy, M.F.; Yossier, N.M. Behavior of beam-high performance fiber reinforced CFST column joints. *Thin Wall. Struct.* **2017**, *113*, 217–227. [[CrossRef](#)]
22. Li, G.-C.; Chen, B.-W.; Yang, Z.-J.; Liu, Y.-P.; Feng, Y.-H. Experimental and numerical behavior of eccentrically loaded square concrete-filled steel tubular long columns made of high-strength steel and concrete. *Thin Wall. Struct.* **2021**, *159*, 107289. [[CrossRef](#)]
23. Pagoulatou, M.; Sheehan, T.; Dai, X.H.; Lam, D. Finite element analysis on the capacity of circular concrete-filled double-skin steel tubular (CFDST) stub columns. *Eng. Struct.* **2014**, *72*, 102–112. [[CrossRef](#)]
24. Ren, Z.; Wang, D.; Li, P. Axial compressive behaviour and confinement effect of round-ended rectangular CFST with different central angles. *Compos. Struct.* **2022**, *285*, 115193. [[CrossRef](#)]
25. Su, R.; Li, X.; Zhong, T.; Zhou, T. Axial behavior of novel CFDST columns with outer welded corrugated steel tubes. *Structures* **2021**, *34*, 2708–2720. [[CrossRef](#)]
26. Sun, Z.-X.; Zou, Y.; Wang, C.-Q.; Pan, J.; Wang, L.; Chen, M. Axial compressive behavior and load-bearing capacity of steel tubular-corrugated steel plate confined concrete composite columns. *Structures* **2022**, *44*, 135–151. [[CrossRef](#)]
27. Sun, Z.; Zou, Y.; Wang, C.; Pan, J.; Wang, L.; Chen, M. Study on confinement mechanism of core concrete in steel tubular-corrugated steel plate confined concrete columns. *J. Build. Eng.* **2022**, *52*, 104497. [[CrossRef](#)]
28. Tang, X.L.; Cai, J.; Chen, Q.J.; Liu, X.P.; He, A. Seismic behaviour of through-beam connection between square CFST columns and RC beams. *J. Constr. Steel Res.* **2016**, *122*, 151–166. [[CrossRef](#)]
29. Tao, Z.; Han, L.H.; Wang, D.Y. Experimental. behaviour of concrete-filled stiffened thin-walled steel tubular columns. *Thin Wall. Struct.* **2007**, *45*, 517–527. [[CrossRef](#)]
30. Tao, Z.; Uy, B.; Han, L.-H.; Wang, Z.-B. Analysis and design of concrete-filled stiffened thin-walled steel tubular columns under axial compression. *Thin Wall. Struct.* **2009**, *47*, 1544–1556. [[CrossRef](#)]
31. Wang, C.; Zou, Y.; Li, T.; Ding, J.; Feng, X.; Lei, T. Ductility and Ultimate Capacity of Concrete-Filled Lattice Rectangular Steel Tube Columns. *Struct. Durab. Health Monit.* **2018**, *12*, 99–110.
32. Wang, F.-C.; Han, L.-H. Analytical behavior of special-shaped CFST stub columns under axial compression. *Thin Wall. Struct.* **2018**, *129*, 404–417. [[CrossRef](#)]
33. Wang, W.; Zhang, L.; Su, S.; Gao, J.; Li, Y.; Li, Y. Experimental research on seismic behavior of corrugated steel plate shear wall. *J. Build. Struct.* **2018**, *39*, 36–44.
34. Wang, Y.; Yang, L.; Yang, H.; Liu, C. Behaviour of concrete-filled corrugated steel tubes under axial compression. *Eng. Struct.* **2019**, *183*, 475–495. [[CrossRef](#)]
35. Wang, Y.T.; Cai, J.; Long, Y.L. Hysteretic behavior of square CFT columns with binding bars. *J. Constr. Steel Res.* **2017**, *131*, 162–175. [[CrossRef](#)]
36. Xu, Y.; Tang, H.Y.; Chen, J.L.; Jia, Y.G.; Liu, R.Z. Numerical analysis of CFRP-confined concrete-filled stainless steel tubular stub columns under axial compression. *J. Build. Eng.* **2021**, *37*, 102130. [[CrossRef](#)]
37. Yang, L.; Wang, Y.; Elchalakani, M.; Fang, Y. Experimental behavior of concrete-filled corrugated steel tubular short columns under eccentric compression and non-uniform confinement. *Eng. Struct.* **2020**, *220*, 111009. [[CrossRef](#)]
38. Yang, M.G.; Cai, C.S.; Chen, Y. Creep performance of concrete-filled steel tubular (CFST) columns and applications to a CFST arch bridge. *Steel Compos. Struct.* **2015**, *19*, 111–129. [[CrossRef](#)]
39. Yang, Y.L.; Wang, Y.Y.; Fu, F. Effect of reinforcement stiffeners on square concrete-filled steel tubular columns subjected to axial compressive load. *Thin Wall Struct* **2014**, *82*, 132–144. [[CrossRef](#)]
40. Ye, Y.; Yun, Z.; Wang, C.; Wu, Y.; Ming, C. Behaviour of concrete-filled horizontal corrugated steel tubular short columns under axial compression. *J. Exp. Mech.* **2021**, *36*, 230–240.
41. Zhou, X.; Lin, X.; Tan, D.; Lu, W.; Yang, L. Fatigue Test of Composite Box Beams with Corrugated Steel Webs. *China J. Highw. Transp.* **2010**, *23*, 33.